

GT2017-64685

**STATISTICAL ANOMALY BASED STUDY OF ROTATING STALL IN A
TRANSONIC AXIAL COMPRESSOR STAGE**

G. S. Heinlein , J. P. Chen
Department of Mechanical and Aerospace
Engineering
The Ohio State University
Columbus, Ohio, United States of America

C. M. Chen, S. Dutta, H. W. Shen
Department of Computer Science and
Engineering
The Ohio State University
Columbus, Ohio, United States of America

ABSTRACT

Tip clearance flow in transonic rotors is known to have a significant effect on compressor performance and stability. The purpose of this study is to employ a novel statistical analysis method as a stall precursor detector and investigate the flow physics underlying stall inception. To allow for natural stall evolution, a full annulus simulation of a transonic axial compressor stage (NASA Stage 35) was performed. Due to the size of the data set, a novel statistical analysis method was employed to rapidly analyze the entire spatial and temporal simulation domain. The analysis method involved utilizing a Grubb's test pointwise on the domain's grid for Entropy to reveal regions, times, and trends that are statistically anomalous and could be of interest for future evaluation. Through use of the anomaly detecting Grubb's test rotating stall, which developed in the stage, could be tracked back in time to immediately after the computed mass flow stabilization of a particular operating condition. It was determined that an 18th order modal behavior dominated the pre-stall regime of NASA stage 35 operating in a near stall condition. The modal behavior was a result of a spiral-type vortex breakdown of the tip clearance vortex after interacting with the passage shock. A rotating disturbance region, moving faster than the rotor speed, amplified an instability within the spiral-type vortex breakdown. The growth of the instability caused the amplitude of the spiral-type vortex breakdown to increase in the radial and circumferential directions. Eventually, the disturbance region broke down into rotating stall due to decreased mass flow rate and high loading. The statistical Grubbs' test of Entropy showed the efficacy of the method at detecting the earliest signs of rotating stall.

INTRODUCTION

The gas turbine operating envelope is limited by the stable operating range of the compressor. It is well known that the rotor tip section contributes significantly to the stability and performance of compressor stages. This is especially true for modern, high tip loaded, transonic compressors since the interactions of the clearance flow, passage shock, and boundary layers can create complex flow structures which interact to induce rotating stall. The flow through the clearance at the blade tips strengthens a vortex formed at the leading edge. As the tip clearance vortex (TCV) progresses in the streamwise direction it interacts with the passage shock inducing breakdown of the vortex. Depending on the operating condition the vortex breakdown can be stable or unstable, an important distinction due to the TCV breakdown affecting the upper portion of the blade passage span. The difficulty in determining the flow phenomena associated to rotating stall is due to the region being problematic for experimental study, which is why there is still a great deal of interest in research of this topic.

Rotating stall is categorized by two different types of inception: short length scale disturbances ("spike") and long length scale disturbances ("modal"). Both modal and spike type stall inception have been experimentally verified to exist in both low and high speed compressors [1-11]. The spike type rotating stall is characterized by having a spike-like appearance in the pressure and velocity traces. Spike stall also has a small circumferential extent and a propagation speed around the annulus of ~60-80% of the rotor speed. As a spike disturbance rapidly increases in size, the rotational rate reduces further, and the mass flow rate decreases rapidly. Camp and Day [3] showed experimentally that spike stall is the localized flow separation occurring when a critical incidence angle in the region is exceeded leading to rotating stall. In addition, spike stall was

determined to be restricted to the tip region of the rotor. Expanding on this idea, a recent paper by Weichert and Day [4] shows the embryonic formation of a spike type stall in low speed compressors begins as a disturbance in the tip clearance vortex. The strength and size of the embryonic disturbance is small enough not to impact neighboring blade passages yet immediately begins to propagate streamwise down the passage upon inception.

The second type of stall inception, or modal stall inception, is characterized by slow growth of long length scale perturbations, in the circumferential direction, up to the order of the annulus. Perturbations in the pressure or velocity field can appear tens to hundreds of revolutions before rotating stall emerges and are indicative of the harmonic oscillations in the flow field. To this end, Hendricks *et al.* [9] determined the overall slope of a compressor's pressure rise characteristic causes modal type stall. Expanding on this general idea of modal stall behavior, Bright *et al.* [2] found that spike behavior can exist on top of modal behavior in the same rotor as it progresses towards stall.

In order to uncover the physical phenomena associated with both stall inception types numerous numerical studies have been performed in the past [12-21]. Yamada *et al.* noted, for simulation of NASA rotor 37, the vortex breakdown in near stall conditions leads to a vortex fluctuation downstream of the shock [12]. This gives rise to unsteadiness in the rotor passage that locally decreases mass flow rate. As the mass flow rate continues to drop, the fluctuation of the vortex breakdown increases which causes interaction with following blades eventually leading to rotating stall. Similarly, Khaleghi [13] found that the blade tip region, and in particular the tip clearance vortex, was responsible for stall initiation by conducting a half annulus simulation. A full annulus simulation of NASA rotor 35, conducted by Chen *et al.* [14], found a full-annulus length-scale disturbance traveled at 100% rotor speed until it devolved into a spike-like disturbance traveling at sub-rotor speeds. Another full-annulus simulation was conducted by Hah *et al.* [15] of transonic fan in a stall condition. The study found that the TCV continues to exist during stall but interactions with the passage shock cause it to oscillate.

The half and full-annulus simulations exemplify a continuing trend in computational work which is to increase the size and complexity of a simulation in order to study fundamental physical phenomena. However, a major problem with this trend is the ever growing size of the data sets which is rapidly becoming prohibitively expensive to perform standard post-analysis. Pertinent information about temporal and spatial trends or unique events are easily overlooked or lost in large scale data sets. To find undiscovered information in large data sets, data mining techniques utilizing some form of statistical analysis are commonly used [22].

Statistical analysis employs various methods to determine outlier data points in a set [23-26]. One common method for detecting outliers in data sets is the Q-test [24] yet suffers in small sets from requiring the actual, and ordinarily unknown, standard deviation. In order to obtain more accurate

outlier determination the Grubbs' test [26] can be employed to limit outlier bias common to small data sets. The Grubbs' test quantifies the required scaling factor given the size of the data set. Utilizing an outlier detection method, anomalous temporal or spatial points are illuminated and can then be investigated through more standard methods. Data mining, in this fashion, allows the rapid and accurate extraction of information as compared to the slow brute force method of investigating the entire temporal and spatial domain of a simulation with standard visualizations.

The purpose of the present work is to utilize a statistical analysis method, the Grubbs' test, as a stall precursor detection method for axial flow turbomachinery. A full-annulus URANS simulation of NASA stage 35 was conducted in a stable, transitional, and fully stalled condition. These cases supplied data to which the statistical Grubbs' test was performed. The purpose is to elucidate trends and regions associated with stall which have previously been unobserved. After trends or events are discovered by the Grubbs' test, standard visualization and analysis techniques are utilized to discover the physical phenomena associated with the outlier points and thereby stall.

NUMERICAL APPROACH AND METHODOLOGY

Numerical Methodology

The current study utilizes the physics simulation code TURBO to solve the unsteady, three dimensional, Reynolds averaged Navier-Stokes equations. The conservative form of the governing equations implemented in TURBO are formulated based on a time marching, finite volume scheme. A Newton iteration scheme was used to discretize time and a cell-centered approach was used to discretize the governing equations spatially. The turbulence model is a realizable two equation k- ϵ turbulence model utilizing a wall integration approach for modeling boundary layers. Further details of the flow solver can be found in Chen and Whitfield [28].

Full annulus simulations of NASA's stage 35, a single stage transonic core compressor, are conducted in the present study. The simulation of the full annulus was chosen for two reasons. The first was to permit the natural formation and progression of the flow field at any specified operating condition; allowing for asymmetric flow features and all length scale disturbances, long length scale (modal) and short length scale (spike), in the circumferential direction to exist and influence the progression of the stage towards stall. The second is to test the efficacy of the statistical analysis method and the full annulus simulation provides an axisymmetric environment such that stall inception can occur in any blade passage at any time. The lack of *a priori* knowledge of the stall inception location will display that the proposed Grubbs' test method is a valuable stall precursor detector.

The full annulus model consisted of 36 rotor blades and 46 stator blades. Each rotor blade passage grid contained 150 cells in the chordwise direction (80 on the blade surface), 70 cells in the spanwise direction (60 on the blade surface), and

55 cells across the blade passage. Each stator blade passages grid contained 140 cells in the axial direction (80 on the blade surface), 70 cells in the radial direction (52 on the blade surface), and 78 cells in the circumferential direction. The simulation grid can be viewed in Figure 1. The top image of Figure 1 is the full annulus model with 1 passage highlighted in the rotor and stator as well as one section of the upstream grid. The bottom image of Figure 1 is a close up of the highlighted passages.

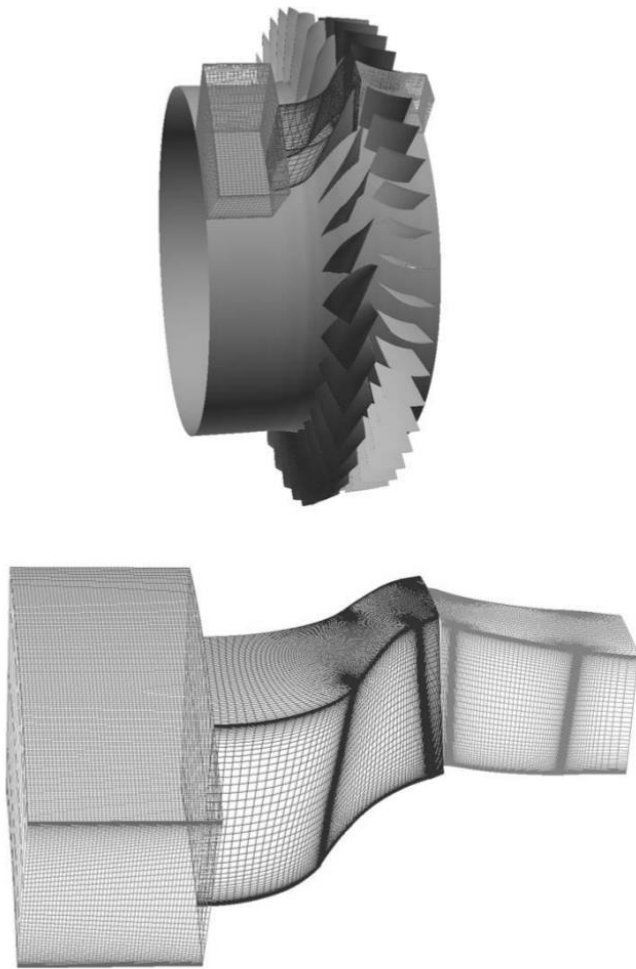


Figure 1. Computational domain for NASA Stage 35. Top – full-annulus domain with one blade passage highlighted, Bottom – close-up view of highlighted blade passage.

The rotor tip gap is 1% of the rotor tip chord employing 10 cells in the radial direction between the tip and casing. The final grid contained approximately 67×10^6 elements. The flow in the tip gap was determined through use of a model and was not explicitly simulated. The clearance model follows that set forth by Kirtley [29] which conserves mass and momentum through the tip gap. While detailed flow physics are not modeled the results are adequate for predicting

the first order effects in strength, extent, and direction Chima [30].

Total pressure and total temperature were prescribed in the spanwise direction at the inlet reflect the total conditions observed at the test facility level. The exit boundary condition was chosen as a “choked” throttle model so that a specified corrected mass flow rate could be given and the static pressure was allowed to float in order to match. An additional note, when the exit boundary condition was changed to match a specified operating condition it was done so in a discrete step rather than a continuous throttling maneuver performed in experiments. Therefore, two rotor revolutions were required for the domain to adjust to the new condition and reach the prescribed mass flow rate.

Placement of the inlet and exit boundary conditions is close to the rotor and stator causing a short upstream and downstream computational domain. The choice of inlet and exit placement was dictated by the additional computational resources, unavailable for the current study, required by creating large upstream and downstream domains. By choosing these locations a surge mode could not be captured due to the lack of a sufficient volume effect. Therefore, any modal disturbance is a result of the blades and the limited volume of the computational domain. The modal activity occurring within the limited volume computational domain can be affected by pressure waves reflecting off of the inlet. Since long-length scale pressure disturbances affect flow significantly far upstream, a large scale disruption of normal activity, on the order of the annulus, could influence the flows progression by interaction with the inlet. However, this work is not endeavoring to capture the entire evolution of modal instabilities into deep stall but resolve physical phenomena caused by the embryonic emergence of instabilities before they increase in size sufficient to interact with the inlet. Thus the use of a small upstream and downstream computational domain was deemed appropriate for use in the current study.

Statistical Analysis Methodology

In order to detect the earliest signs of stall from large data sets a pointwise statistical analysis technique was developed by Chen *et al.* [27]. The technique capitalized on the axisymmetric nature of the full annulus simulation such that every blade passage has the exact same grid. As an example, consider a grid element (i.e. a cell volume) on the surface of the blade. This element has 35 other grid elements corresponding to the exact same locations relative to the other blades. The symmetry allows every grid element within a blade passage to be grouped into a set of 36, due to there being 36 blade passages. The result of the grouping yields $150 \times 70 \times 55$ unique sets of 36 points for the full annulus rotor domain. Any scalar variable (i.e. pressure, temperature, Entropy, etc.) can be investigated because each grid element contains every solution variable. Each set was then analyzed with the statistical Grubbs’ test using one of the scalar variables selected by the user.

A Grubbs’ test is used to detect outliers in a single variable data set in a similar method as the Q-test. The process

of the Grubbs' test involves finding the distance of a point, in a set, from the mean of that set, in terms of the standard deviation. The Grubbs' test is shown in Equation 1 where Y_i is a point of the set, \bar{Y} and σ are the mean and standard deviation of the set respectively, and G_i is the value of the Grubbs' test for that point

$$G_i = \frac{Y_i - \bar{Y}}{\sigma} \quad (1)$$

From this test a point is considered to be an outlier if its value G_i is greater than 3.3 based on the criteria described in Chen *et al.* [27]. The Grubbs' test was performed pointwise within the domain and the outlier points were cataloged by their associated tangential location and blade passage number. Since the statistical analysis, Grubbs' test, detects outliers significantly far from the mean the results of the analysis will be referred to in the remainder of the paper as "anomalies". The results from the analysis produced a total number of outlier points (anomalies) per blade passage for a given time step. The analysis was performed on the entire rotor every 25th computational time step, which resulted in 144 statistical analyses per revolution. One issue in associating an outlier point with its corresponding tangential location and blade passage is the loss of radial and axial spatial information.

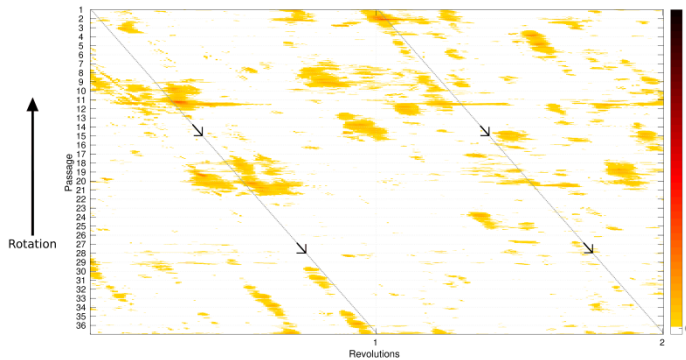


Figure 2. Statistical outlier analysis of Entropy, in the relative frame, for the stable flow condition 20.35 kg/s

However, this novel method of analysis allows for the rapid visualization of the rotor section over the entire simulation time in the form of a 2D heatmap. Spatial regions containing a large number of anomalies can be later investigated with standard methods to reveal phenomena within the rotor passage. Figure 2 is the heatmap of the stable flow condition 20.35 kg/s and displays the circumferential location versus simulation time step, in revolutions.

On viewing the anomaly heatmap of the statistical analysis data, Figure 2 as an example, there are a few key pieces of information that need to be kept in mind: (1) y-axis is the circumferential location of the data with the corresponding blade passage number overlaid. (2) The anomaly heatmap is the 'unrolled' version (i.e. blade passages 1 and 36 connected) of the rotor for all time steps which results in a relative

reference frame viewpoint. The rotation direction on the left side displays the motion of the rotor (3) The black lines crossing the heatmap displays the motion of a point in the inertial frame (e.g. a casing pressure tap) viewed in the relative frame with arrows showing direction. (4) As the heatmap color becomes darker, more points of the chosen scalar variable (in the current case Entropy) have been labeled as anomalies within the region.

Comparison with Measured Data

Pertinent details of NASA's Stage 35, shown in part on Table 1, were provided in Reid and Moore [1]. The rotor of Stage 35 is designed to be a tip loaded transonic blade. The relevant experimental work on Stage 35 was performed by Bright *et al.* [2] and Weigl *et al.* [11]; they conducted tests on a high-speed compressor at 85% and 100% design speeds respectively. Particular emphasis will be given to the clean inlet flow condition as it is of the most interest to this study. For the clean inlet case, based on pressure transducer data, Bright *et al.* [2] concluded that the compressor stalls due to modal instabilities with additional spike-type instabilities present just prior to stall.

Table 1: Design specifications of the compressor stage

Rotor speed at 100% (rpm)	17188.7
Tip speed (m/s)	454.46
Hub/tip ratio	0.7
Rotor aspect ratio	1.19
Stator aspect ratio	1.26
Solidity at tip	1.288
Number of rotor blades	36
Number of stator blades	46

Validation of the current full annulus model for NASA Stage 35 has occurred previously in the works of Chen *et al.* [14]. Figure 3 shows the computed and experimental speed lines for mass flow rate versus total-to-static pressure ratio at the design speed.

The computed pressure ratio can be observed to be higher for the computational simulations than those obtained through experiment. The discrepancies are most likely due to differences in the tip gap size of the actual compressor at design speed versus the computational grid which displays a fixed height with no variation. However, Figure 3 displays the correct slope which is the crucial parameter in stall inception and correlates to the modal type stall inception observed in experiment.

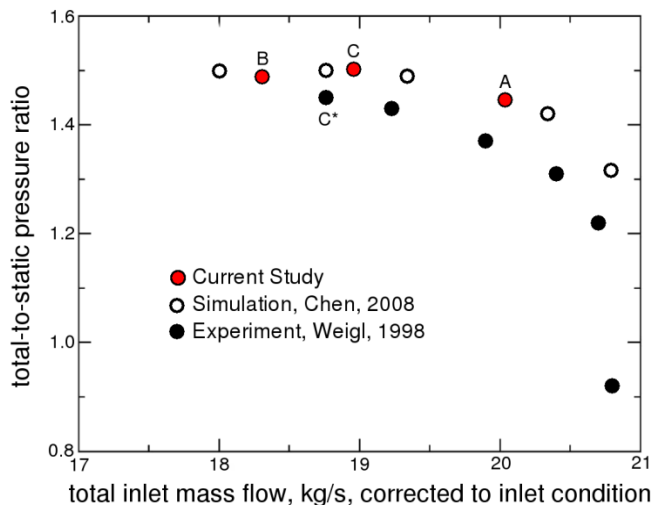


Figure 3. Experimental and simulated speed-lines, at design speed, of NASA stage 35

In the current study, three test cases were conducted, labeled A – C, shown in Figure 3. Figure 3 also displays the experimental data of Weigl *et al.* [11] and previously simulated data of Chen *et al.* [14]. The three test cases correspond to the three operating conditions: (A) A stable flow condition (20.35 kg/s) which will never lead to stall; (B) An unstable flow condition (18.34 kg/s) that rapidly advances to a rotating stall state; (C) A transitional flow condition on the stable side of the speed line near the predicted stall point (18.89 kg/s). Simulation C is labeled as “transitional” due to the proximity to maximum total to static pressure ratio and the modal stalling nature of Stage 35, and C* being the predicted stalling point given for the stage given by Weigl *et al.* [11]. The stable and unstable flow condition cases were conducted to assess trends in the statistical analysis and provide insight during the investigation of the transitional flow condition.

RESULTS AND DISCUSSION

Stable Condition

In order to gain a greater understanding of the trends and flow physics associated with the results of the statistical analysis, a stable and a stalled operating condition will initially be examined. The stable operating condition, 20.35 kg/s, will be investigated first and can be seen as flow condition, A, in Figure 3. The trends uncovered in the anomaly analysis can be associated with a stable operating condition. The anomaly analysis was performed using Entropy as the scalar variable of interest for every 25th simulation time step. As previously stated the anomaly analysis, or Grubbs’ test, detects outliers from a set of scalars. The set is formed of grid points in the same relative location in each blade passage because all blade passages are symmetric. An outlier is detected when the Grubbs’ value of a point is 3.3 standard deviations away from the average of its set. The stable condition simulation was run for two revolutions after the mass flow stabilized to the specified level. This

provided ample time for trends to emerge indicative of stable flow which can be leveraged when examining future simulations.

The results of the statistical analysis produced Figure 2 which displays the heatmap of circumferential location, viewed in the relative frame, versus simulation time in revolutions. Because the axial and radial locations cannot be shown, the heatmap signifies the total number of points at every tangential location (i.e. the sum of all axial and radial anomalous points at their respective tangential locations). It can be observed in Figure 2 no significantly long lived trend emerges in the statistical analysis and the detected outliers are mainly confined to a particular blade passage. Further investigation of the detected anomalies from the full data set, at various time steps, shows no tendency for a particular axial or radial region in a blade passage. Therefore, the points that exhibit statistical anomalies in this stable condition are caused by unsteadiness inherent in the simulations.

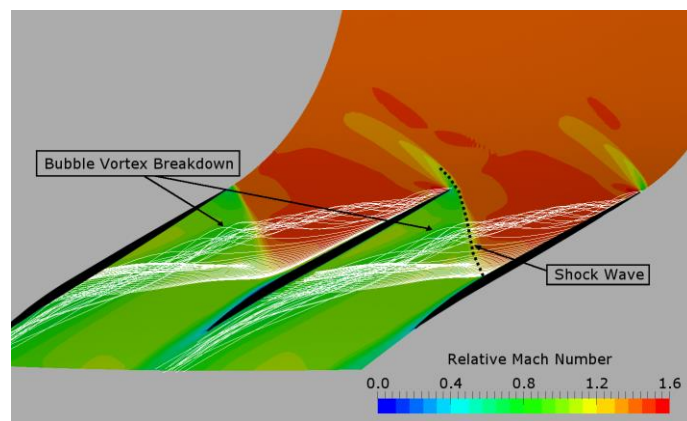


Figure 4. Relative Mach number contour at 98% span with streamlines of the tip clearance flow for the flow condition 20.35 kg/s

Previous studies have identified the tip region, and the tip clearance vortex, TCV, breakdown in particular, as the cause of rotating stall in Stage 35 [12,15,18]. There are two main types of vortex breakdown, the bubble-type and spiral-type, that can be exhibited by the TCV. The bubble-type vortex breakdown is a nearly axisymmetric bubble-like structure occurring due to the expansion of the vortex core upon rapid deceleration. The spiral-type vortex breakdown is the deformation of the vortex centerline into a corkscrew or helical-like structure which exhibits less expansion in the size of the vortex core. Both breakdowns occur due to the sudden deceleration of axial velocity and its redistribution into the radial and circumferential direction to maintain mass and vorticity [32-35]. Focusing on the tip region and investigating flow structures located within the outer portion of the span highlight a stable operating condition which will be used for comparison in later test cases.

Figure 4 shows the Mach number contour at 98% span with streamlines emanating from the tip clearance gap in order to highlight the TCV. The TCV can be observed as a tight spiral extending from the leading edge and being strengthened by the

clearance flow. As the TCV progresses down the passage it can be seen to interact with the oblique passage shock caused by the following blade. The shock/vortex interaction is almost perpendicular and causes the TCV to breakdown in a bubble-type manner, shown as the expansion of the streamlines.

Unstable (Stalled) Condition

The second simulation is shown as flow condition, B, in Figure 3 was of the unstable, or stalled, operating condition case with a prescribed mass flow rate of 18.34 kg/s. The unstable condition provides context on trends exhibited by the statistical analysis associated with stall. The mass flow rate history for this unstable case is shown in Figure 5. A constant mass flow rate is present in the early revolutions of the simulation, however, approximately 2.5 revolutions into the simulation the mass flow rate dramatically drops off which is consistent with known rotating stall behavior. The simulation is then terminated soon after due to the current study being focused on stall precursors and initiation and not that of simulating deep stall conditions.

The results of the anomaly analysis produce Figure 6 which is the heatmap of the detected outlier points. Again, it should be noted that the darker the coloring the more points in that particular circumferential location were detected as outliers. With this in mind, two general trends are apparent in the anomaly map that were not present for the stable flow condition: 1) A persistent spatial region, approximately half the annulus, containing a large number of outlier points and 2) Negative sloped temporal trends affecting multiple blade passages over time that eventually lead to a coalesced region at the end of the simulation.

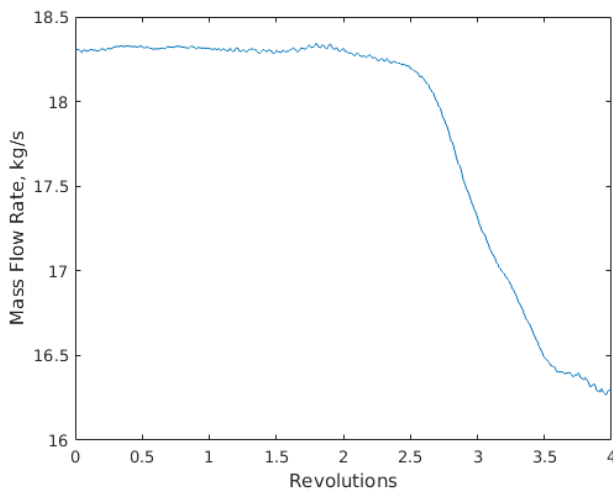


Figure 5. Mass flow rate history off the unstable flow condition 18.34 kg/s

The persistent spatial region affecting approximately half of the annulus comprised of the detected outlier points in a negative sloped pattern. The spatial region formed of

anomalous points in negative sloped trends will be termed the disturbance region for the remainder of the paper. The half-annulus disturbance is sustained until eventually coalescing into a single negatively sloped region around revolution two and a half. The coalesced negatively sloped trend, displaying spatial and temporal persistence, corresponds to the drop in mass flow rate observed at the same time in Figure 5. The coalesced region is propagating around the annulus at ~60% rotor speed in the inertial frame (or 40% rotor speed against the rotor rotation direction in the relative frame). The combination of mass flow rate drop and propagation speed is consistent with typical rotating stall.

The negative sloped temporal trends sporadically affecting multiple blade passages appear to form in a pattern of individual trails that affect one blade passage before being transferred to the next until they dissipate. The individual trends propagate from one passage to the next at ~45% of the rotor speed in the inertial frame (or ~55% rotor speed against the rotor rotation direction in the relative frame). Investigating the physical location of the outlier points shows the majority are in the tip region of the effected blade passages. The combination of propagation from blade passage to blade passage and the tip region being affected is a behavior reminiscent of a rotating instability and will be investigated in depth in the next section of the paper.

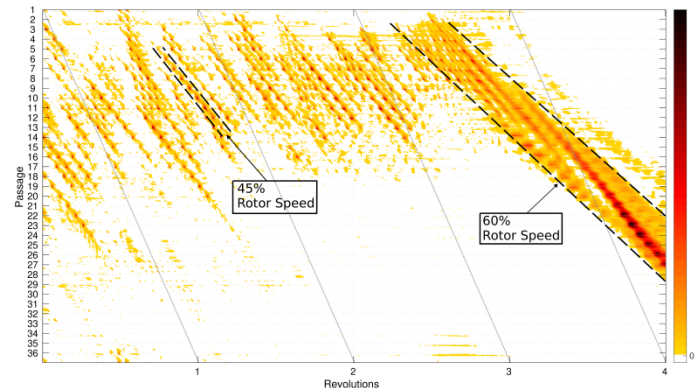


Figure 6. Statistical outlier analysis of Entropy, in the relative frame, for the unstable flow condition 18.34 kg/s

Transitional Condition

With the stable and unstable operating conditions effectively bounding the interpretation of the trends observed in the statistical anomaly analysis, the transition condition of 18.89 kg/s was investigated. The transitional condition can be seen as flow condition, C, in Figure 2. The transitional case was initialized from the stable 20.35 kg/s case through a step change in mass flow rate of the exit boundary condition. After mass flow stabilization the simulation progressed for 18 more revolutions until the mass flow rate dropped, in the same way as observed Figure 5, and was ended. Figure 7 is the heatmap of the statistical analysis of outliers plotted as circumferential location versus simulation time in revolutions.

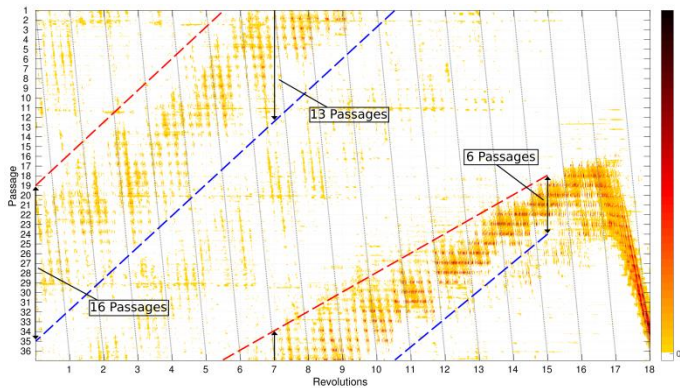


Figure 7. Statistical outlier analysis of Entropy, in the relative frame, for the transitional flow condition 18.89 kg/s

Figure 7 is similar to the unstable case in that a disturbance region formed of negative sloped temporal trends affecting multiple blade passages emerges. Eventually the disturbance region coalesces into a single negative trend occurring simultaneously with a significant drop in mass flow rate, indicating rotating stall. Unlike the unstable case, which only has a fixed spatial disturbance region before rotating stall, the current case has a positive sloped temporal and spatial trend formed by the disturbance region occurring before stall. In Figure 7 the red dashed line denotes the upper extent of the main disturbance region and the blue line denotes the lower extent of the main disturbance region. The extent of the disturbance region can be seen to decrease as stall is approached, shown as the limiting line approaching one another. Three distinct aspects of Figure 7 will be addressed in the following sections: (1) the negative sloped trends forming the disturbance region, (2) the decreasing circumferential extent of the disturbance region, and (3) the positive sloped progression of the disturbance region.

Negative Sloped Trends of the Disturbance

The negative sloped outlier trends form the disturbance region and propagate from passage to passage at $\sim 15\%$ rotor speed in the inertial frame (or 85% rotor speed against the rotor rotation direction in the relative frame). These trends are present immediately after mass flow stabilization 16.5 revolutions before the onset of rotating stall (revolution 0). The disturbance region, and the negative sloped trends that form it, can be seen propagate faster than the rotor and form the positive sloped trend. Following the path of the positive sloped trend taken by the disturbance region eventually leads to rotating stall. Therefore, in the same manner as the unstable flow condition, the negative sloped trends forming the disturbance region lead to stall.

The physical location of the detected outlier points in the disturbance region is concentrated in the tip region of the blade passages. The location of the detected outlier points is consistent with previous findings that highlight the tip region as contributing significantly to stall in transonic rotors. An investigation of the tip region was conducted at several time

steps throughout the simulation to determine specific flow phenomena associated with the outliers determined by the anomaly analysis.

Figure 8 shows the relative Mach number contour at 98% span with streamlines emanating from the tip clearance gap at revolution 14. The findings from the streamline analysis of the TCV and relative Mach number contours reveal a cyclic fluctuation in the vortex and subsequent spiral-type breakdown downstream of interacting with the passage shock. In the past spiral breakdown of the tip clearance vortex when operating in near stall conditions has been computationally shown for transonic rotors [12,18].

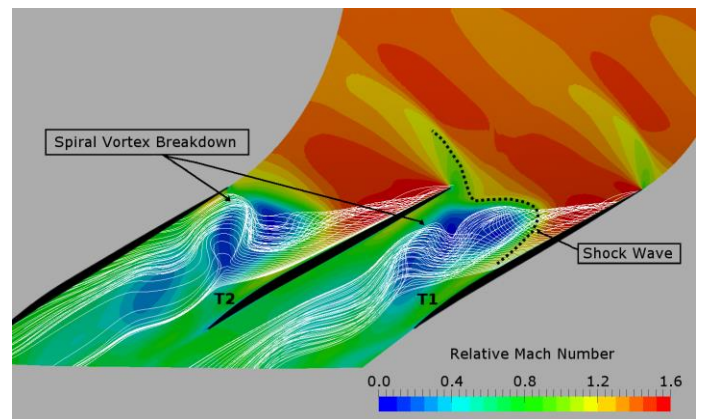


Figure 8. Relative Mach number contour at 98% span with streamlines of the tip clearance flow for the flow condition 18.89 kg/s at revolution 14

A detached bow shock can be observed ahead of the blades, highlighted as the passage shock system in a red dashed line. The TCV no longer interacts with the shock in a perpendicular manner as in Figure 4, the stable operating condition. The vortex breakdown is now of a spiral-type and oscillates mainly in a plane of constant span. A large low momentum region in the center of the passage downstream of the shock is created by the vortex breakdown. The radial, or spanwise, extent of the low momentum region is affected by the position of spiral breakdown and passage shock. Coupling exists between the vortex breakdown, low momentum fluid, and shock position all of which act to influence the respective position of one another during oscillation of the TCV and vortex breakdown.

The two spiral vortex breakdowns in Figure 8 are labeled as, T1, on the right blade passage and, T2, on the left blade passage correspond respectively with the maximum and minimum upstream positions of the TCV during its oscillation in a plane of constant span. For each blade passage during one oscillation cycle the TCV, and subsequent breakdown, experience both positions T1 and T2.

In order to elucidate the important behavior of the vortex breakdown system of a single passage, Figure 9 displays a representative sketch of the TCV and vortex breakdown at two times during its oscillation cycle. Boundary layer effects are removed as they complicate and smear out the physical

phenomena of vortex breakdown. The vortex breakdown system at the first time instance of its oscillation, shown as the red vortex in Figure 9, is the representation of the labeled region T1 in Figure 8. The vortex breakdown system at the second time instance of its oscillation, shown as the black vortex in Figure 9, is the representation of the labeled region T2 in Figure 8.

The vortex system shown in red corresponds to the maximum upstream position of the TCV after interaction with the passage shock, noted as the first time instance. As previously stated, the vortex breakdown causes a low momentum region, or blockage, to exist just downstream of the passage shock. The spiral breakdown at this time is at its lowest circumferential extent, furthest from the pressure side of the following blade, due to the nature of the spiral motion. Therefore, the influence on the following blade is at a minimum as a result of the position of the vortex system shown in red. Incoming flow is able to partially divert in the axial direction along the pressure side of the following blade effectively decreasing the loading.

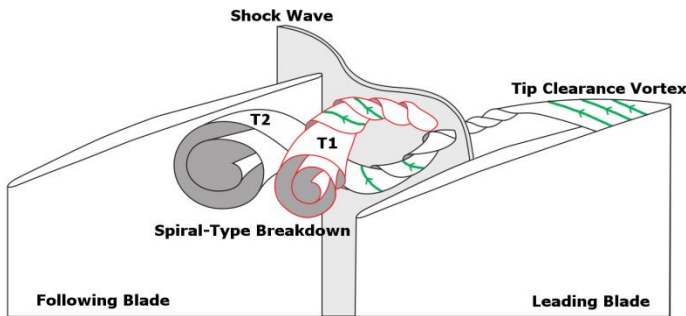


Figure 9. Representative sketch of the tip clearance vortex spiral-type breakdown and resulting instability growth mechanism for the flow condition 18.89 kg/s

The progression of the oscillation cycle brings the downstream motion of the TCV, shown in red, until it becomes the vortex system shown in black. This system is noted as the second time instance and corresponds to the minimum upstream position of the TCV after interaction with the passage shock. The spiral breakdown at this time is at its largest circumferential extent due to the nature of the spiral motion. The influence on the following blade is additionally at a maximum due to the blockage, the low momentum region, caused by the breakdown being located next to the pressure side of the following blade. Loading on the following blade is increased due to flow responding to the blockage by diverting in a more tangential direction.

As the oscillation cycle continues the vortex system shown in black will advance once again becoming the red vortex system. During this time the TCV progresses upstream and the motion of the spiral breakdown progresses away from the pressure side of the following blade. Additionally, the low momentum region caused by the spiral breakdown of the

system shown in black propagates streamwise along the passage.

The illustration and explanation of the behavior in the TCV oscillations also explains the negative sloped trends observed in the disturbance region throughout the pre-rotating stall revolutions (before ~ 16.5 rev). The negative sloped trends observed in the anomaly heatmap of Figure 7, is a result of larger than average low momentum region occurring due to the spiral-type vortex breakdown which are then passed to the following blade passage during the oscillatory motion. These low momentum regions propagate circumferentially toward the following blade and then streamwise along the passage, as shown in Figure 9. As the low momentum fluid moves next to the following blade, the black vortex system in Figure 9, it causes a localized change in loading at the leading edge of the following blade. The result is a larger than average low momentum region appearing in the following blade passage. This propagation continues to influence the following blades in a manner very similar to stall cell propagation until the strength dissipates and no longer affects the following blades to the extent that an outlier is detected. The disturbance passing does not have a significant enough strength to induce rotating stall early in the simulation and is similar to the embryonic spike stall formation described in Weichert and Day [4].

Decreasing Size of Disturbance Region

The circumferential size of the disturbance region can be observed to change over the course of the simulation. Figure 7 highlights the change in disturbance size as the convergence of the upper extent of the disturbance, shown as the red dashed line in Figure 7, and the lower extent of the disturbance, shown as the blue dashed line in Figure 7. Early in the simulation the disturbance region is approximately half annulus in extent, ~ 16 blade passages, but as stall is approach the extent is approximately a sixth of the annulus, ~ 6 blade passages.

Figure 10 displays the representation of the relative motion and decrease in size of the disturbance region shown in Figure 7. The viewing perspective of Figure 10 is streamwise along the axis of rotation in the relative reference frame. The disturbance size and location of the majority of detected outlier points, highlighted in red, are shown at two different simulation times, 0th revolution (top) and 15th revolution (bottom). In both of the images of Figure 10 the disturbance region is mainly located in the top 10% of the span, specifically, near the TCV.

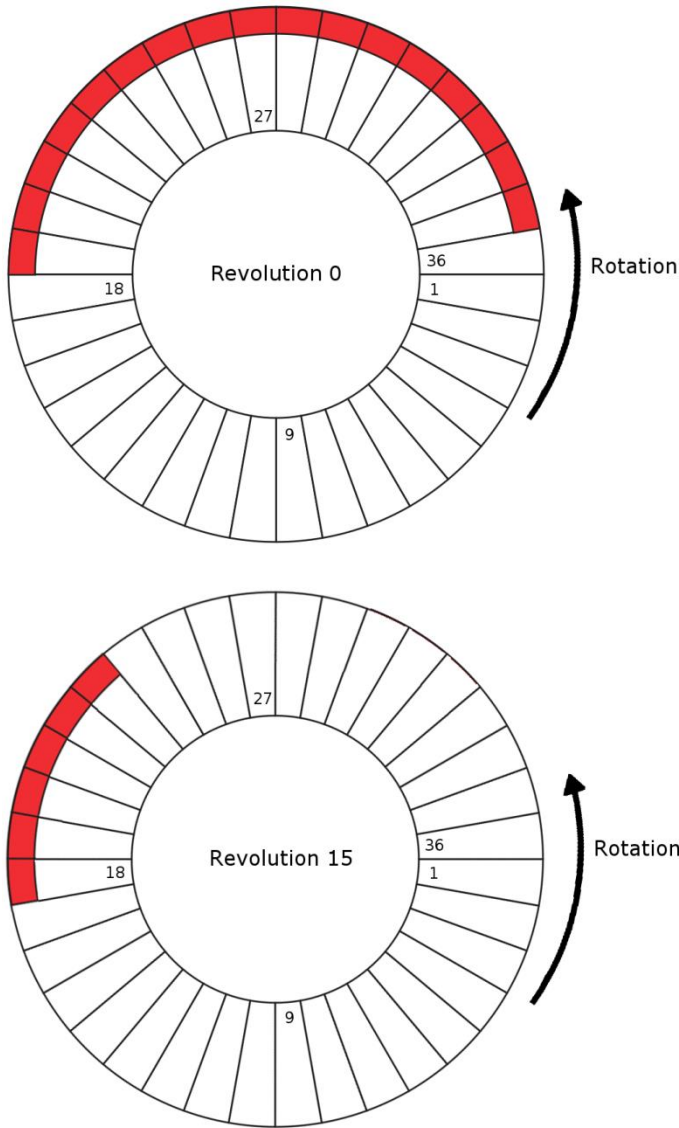


Figure 10. Size and relative location of the disturbance region at (top) revolution 0 and (bottom) revolution 15

At revolution 0 the circumferential extent of the disturbance in the top image of Figure 10 is almost half the annulus (blade passages 19 - 35). It should be noted that the detected regions of outlier points are sparse in the highlighted during this time period, which can be observed in Figure 7. Marked changes can be noticed as the simulation progress towards stall shown in 15th revolution. The circumferential extent of the disturbance has decreased to almost a third of its former size and the density of detected outliers in the highlighted region is higher, also observable in Figure 7. The disturbance region is therefore coalescing and growing in strength as stall is approached.

The reason for the change in size and strength of the disturbance region can be found in the evolution of the instability of the tip clearance vortex and vortex breakdown. After mass flow stabilization, when the disturbance region is

approximately half annulus in size, the simulation possesses an 18th order modal behavior. This is a full annulus phenomenon in the circumferential direction which possesses a wavelength of two blade passages. The two blade passage pair emerges around the rotor annulus in the tip region as opposing oscillations in the tip clearance vortex. Meaning, as the vortex breakdown reached it largest circumferential extent in one blade passage (shown as T2 in Figure 8 and the black vortex in Figure 9), the paired blade passages had their respective vortex breakdowns at the smallest circumferential extent (shown as T1 in Figure 8 and the red vortex in Figure 9).

Initially the modal behavior caused by the oscillatory motion of the TCV and vortex breakdown was present in every pair of passages around the annulus. During the early revolutions of the simulation visual inspection of the domain through streamlines, contours, and section planes displayed remarkable similarity among all pairs and hence is difficult to detect signs of stall. However, as evidenced in Figure 7, sign of stall show up as soon as the simulation has stabilized to the prescribed mass flow rate (revolution 0). This provides evidence as to the efficacy of the statistical analysis as a stall precursor.

As the simulation progressed, instability growth was exhibited by the TCV and vortex breakdown within the disturbance region. The 2nd revolution displayed the disturbance region passages differentiated themselves from the opposite side of the rotor. Figure 11 displays the relative Mach contours and TCV streamlines for a pair of blade passages from the disturbance region at the 2nd revolution. The amplitude of oscillations and the strength of the velocity deficit in the low momentum region caused by the vortex breakdown grew on the side of the rotor containing the detected disturbance region. While at the same time the opposite side of the rotor displayed little change in the behavior flow of the tip region.

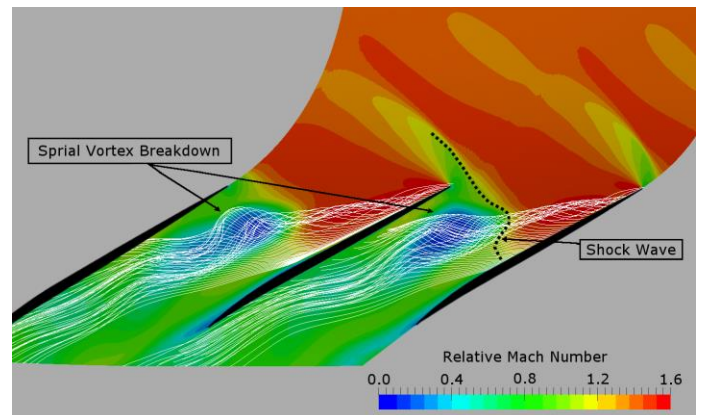


Figure 11. Relative Mach number contour at 98% span with streamlines of the tip clearance flow for the flow condition 18.89 kg/s at revolution 2

As the simulation progressed slow instability growth continued in the disturbance region causing further increases in the oscillation amplitude of the TCV and vortex breakdown. The low momentum region caused by the breakdown also

exhibited increase in size and velocity deficit, i.e. a blockage, in the disturbance region. A larger blockage causes greater impedance to the flow near the disturbance center and lower impedance near the edges, decreasing the size of the disturbance region. This can be seen in Figure 7 that the 7th revolution shows a 20% decrease in the disturbance size or approximately 1 passage every 2 revolutions.

After the 7th revolution the rate of change in the size of the disturbance began to increase, showing approximately 1 passage of decrease per revolution until stall. The core of the disturbance region displayed continued instability growth, whereas, the opposite side of the rotor showed a decrease in the strength of the oscillations. This behavior of the rotor continued until the full annulus modal behavior broke down approximately at the 12th revolution.

The disturbance region exhibited a breakdown in the two passage length pairing of the TCV and vortex breakdown oscillations. The oscillatory behavior of the tip region became more erratic and no longer possessed the two blade passage pairing. The cause of the change is likely due to the increase size and mass of the blockage in the disturbance blade passages. This difference can be observed by comparing the low momentum in the disturbance region of Figure 11 (early revolution behavior) to those exhibited by Figure 8 (late revolution behavior). The blockage caused by the low momentum region can be observed to have increased significantly in size with progression of the simulation.

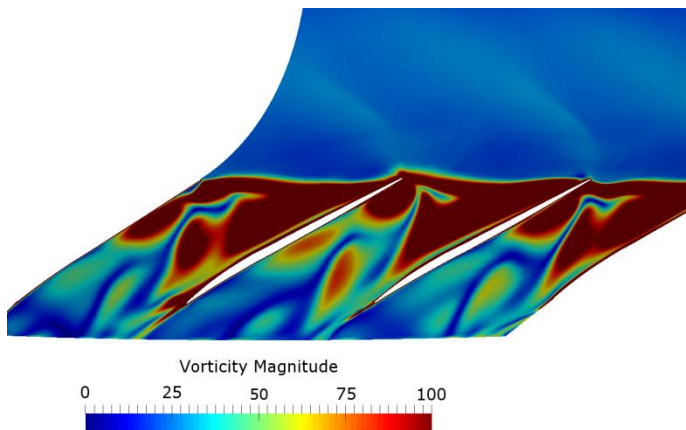


Figure 12. Contours of vorticity magnitude at 98% span at revolution 14

The large blockage (low momentum region) increased mass in the tip region. Increases in mass change the harmonic nature of the flow in the tip region which adjusted to a new state, i.e. natural frequencies, in an analogous way to increasing the mass of a mass-spring system changes the natural frequency. The result is the observed breakdown of previous modal behavior in the disturbance region. Outside of the disturbance region the same two blade passage behavior continued providing further evidence that the disruption in modal behavior is related to the mass of the blockage.

As mentioned previously the behavior of the TCV and vortex breakdown at the 12th revolution became more erratic. This was due to the oscillation amplitude of the vortex breakdown being too large to maintain the previously observed oscillatory behavior and detached eddies began to form. As the spiral breakdown oscillates to its lowest streamwise extent (shown as T2 in Figure 8 and the black vortex in Figure 9) the vortex tube cannot sustain the motion and will wrap around on itself to form a detached eddy.

Figure 12 displays the vorticity magnitude at 98% span in the disturbance region at revolution 14. The detached eddies can be observed as packets of high vorticity downstream of the vortex breakdown. Once separated from the breakdown the detached eddies propagate streamwise down the passage reducing in strength due to dissipation and flow deceleration. In addition, the formation of a detached eddy causes increased blockage in the effected blade passages.

Interaction between blades in the disturbance area is also increased as the tip region behavior changes resulting in increased blockage to the flow. The larger blockage in the disturbance region causes further reduction to the size and the resultant increased flow impedance causes more flow to divert to other portions of the annulus. At the 14th revolution the opposite side of the annulus was observed to no longer possess oscillatory behavior in the TCV and vortex breakdown. The structure of the tip region, opposite the disturbance, after the 14th revolution was similar to the stable condition shown in Figure 4.

From 14 - 16.5 rev, the disturbance region displayed continued growth of the spiral-type vortex breakdown causing detached eddies to propagate downstream. Whereas, the opposite side of the annulus showed very little change in the behavior due to the blade passages being in a stable condition. This behavior can be observed in Figure 7 as the disturbance region displayed a greater density of outlier points and the remainder of the annulus displayed only a few sporadic outliers.

Positive Sloped Trend of Disturbance Region

The negative sloped trends forming the disturbance region, as well as, the decreasing size of the disturbance region can be seen to have relative motion in Figure 7. The positive sloped trend is associated with the forward propagation the disturbance region that eventually leads to rotating stall. The speed of the forward disturbance propagation is faster than the rotor speed, approximately ~105% rotor speed, which to the authors knowledge, has not been observed before in computational simulations or experimental studies of transonic rotors. While the propagation of the disturbance region leading to rotating stall at a speed faster than the rotor has not been observed it can be explained by two main factors: (1) increased loading at the tip ahead of the disturbance region resulting in a rotor imbalance and (2) a perfectly symmetric geometry of the full annulus model.

To observe loading in the blade tip region (i.e. >95% span) the diffusion factor, DF, as set out in Suder *et al.* [10],

will be utilized. The diffusion factor is calculated in Equation 2 as:

$$DF = 1.0 - \frac{\overline{W_{out}}}{\overline{W_{in}}} + \frac{\Delta \overline{W_{\theta}}}{2\sigma \overline{W_{in}}} \quad (2)$$

Where $\overline{W_{out}}$, $\overline{W_{in}}$, and $\overline{W_{\theta}}$ are the mass-averaged rotor relative exit, inlet, and circumferential velocity, respectively, and σ is the rotor solidity. A near critical loading diffusion factor, $DF = 0.65$, will be subtracted from the calculated diffusion value to emphasize the differences between the stability of each blade passage in the rotor. Additionally, a time averaging of two blade passing periods will be employed due to the unsteady nature of the simulation and desire to capture the cyclic behavior of the TCv. Figure 13 displays the polar plot of the diffusion factor as the distance in the radial direction versus the blade passage number in the tangential direction. The diffusion factor was calculated at the 10th revolution of the simulation. The blade passages detected by the statistical analysis at the 10th revolution are highlighted in red (passages 29-35).

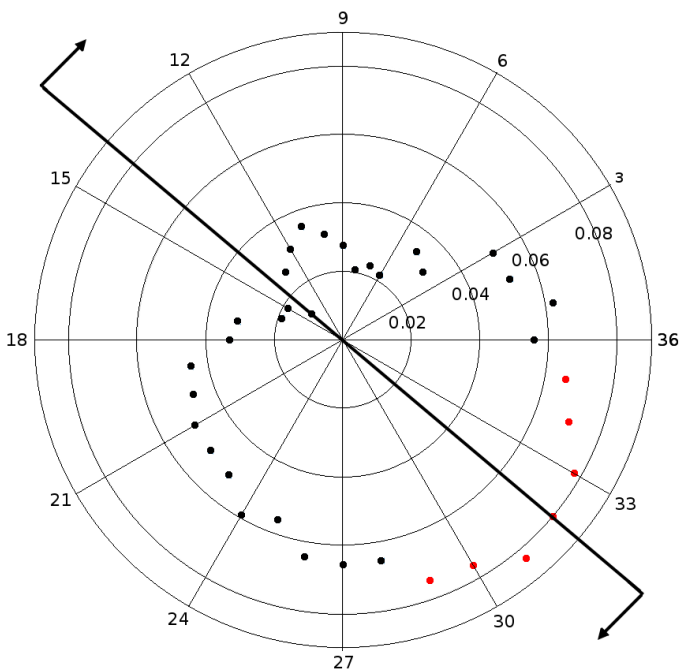


Figure 13 Polar plot of normalized diffusion factor in the tip region versus blade passage. A half annulus dividing line splitting the detected disturbance region marked as red dots

The line crossing the plot of Figure 13 separates half of the rotor by bisecting the disturbance region with the arrows pointing in the direction of rotation. What can be observed is the highest blade loading occurs in the disturbance region and the lowest blade loading occurs in the passages on the opposite side of the annulus. The blade passages (15 - 28) ahead of the disturbance, or below the line, can be seen to be higher than those above the line, or behind the disturbance (13 - 36),

causing an imbalance of loading in the rotor. A higher diffusion factor, corresponding to higher loading in the tip region, is a result of higher axial deceleration and an increase in the axial pressure gradient.

In a low loading condition there is a stabilizing mechanism keeping the size of the vortex breakdown from growing. The stabilizing effect emerges from flow being able to accelerate around the blockage caused by the breakdown. Acceleration around the breakdown acts to reduce the axial pressure gradient reducing the redistribution of mass to the circumferential and radial directions, thereby decreasing the strength of the breakdown. Conversely, in a higher loading condition, the vortex breakdown can continue to grow, though not without limit, because the balancing mechanism no longer as effective. Higher loading decreases the ability of the flow to accelerate around the blockage due to the higher axial pressure gradient. The redistribution of mass from the axial into the radial and circumferential directions further destabilizes vortex breakdown and allows for continued growth.

Utilizing the previous explanation, the forward motion of the detected disturbance region can be explained by the imbalance in the loading of the rotor. The blade passages ahead of the disturbance are continuously being destabilized by the higher loading. Whereas, the blade passages behind are continuously being stabilized by the lower loading. Forward motion of the disturbance region is therefore a result of these two unbalanced loading conditions occurring on opposite sides of the disturbance.

There are many reasons as to why the faster than rotor speed disturbance has not been experimentally observed. The most compelling is a geometric inconsistency (e.g., unequal tip clearance, stagger angle, casing irregularity, etc.). In many experimental studies [2-11] it has been observed that there exists a preferential tendency for the stall inception point in a particular circumferential region of the annulus or even in a particular blade passage. Geometric inconsistencies in the annulus could cause unnaturally high loading in a particular blade passage or region. The resulting passage or region would continually show the highest loading, fixating the imbalance, and preventing the forward propagation of the disturbance. The different in the current computational simulation is that the annulus and each blade passage are perfectly symmetric. This means that there exist no such preferential locations for stall to form or be under continuous influence by the geometry.

A novel statistical analysis technique, the Grubbs' test, uncovered two distinct trends in the transition condition that were associated with stall. The first was a disturbance region showing the propagation from blade passage to blade passage of larger than average low momentum regions at ~15% rotor speed. This phenomenon was caused by the oscillation in the spiral-type vortex breakdown of the TCv and closely resembles the propagation mechanism of rotating stall. The second was the forward propagation of the disturbance region in the relative frame which is the result of imbalanced loading in the rotor tip region.

CONCLUSIONS

A full-annulus URANS simulation of NASA stage 35 in a near stall condition was conducted in order to utilize a statistical anomaly detection method as a stall precursor. The results of the investigation are as follows:

1) A novel anomaly analysis method, utilizing a statistical Grubbs' test, was performed on a full-annulus simulation of NASA stage 35 and was used as a stall precursor to detect the earliest signs of rotating stall. The efficacy of the method was proven by signs of flow instability being traced back to the earliest moments after the simulation stabilized to the prescribed condition.

2) The trends discovered by the anomaly analysis, Grubbs' test, clearly show rotating stall being detected concurrently with the well-established mass flow rate decrease associated with rotating stall. Additionally, a positive trend (moving faster than the rotor speed) and negative sloped trends (moving slower than the rotor speed) were uncovered.

3) The trends moving slower than rotor speed are the result of larger than average blockage in a blade passage influencing the following blade passage during the oscillations in the breakdown of the tip clearance vortex. The following blade passage would then display larger than average low momentum regions and this type of passing would continue until dissipation damps it out, a mechanism similar to stall cell passing.

4) Over time growth in the amplitude of the tip clearance vortex oscillations resulted in locally decreased mass flow rate and coalescing of the disturbance region. Stall was initiated when the size of the blockage could no longer be supported and a rotating stall cell emerged traveling at ~60% of the rotor speed.

5) A trend moving faster than the rotor speed, ~105%, also was exposed during the statistical analysis. Higher loading and axial pressure gradient in front of the disturbance region, and opposite behind, caused a rotor imbalance resulting in the forward propagation of the disturbance.

ACKNOWLEDGMENTS

This work was supported in part by NSF grants IIS-1250752, IIS-1065025, program manager Almadena Chthelkanove, and US Department of Energy grants DE-SC0007444, DE-DC0012495, program manager Lucy Nowell. Additionally, this work was supported by the Ohio Supercomputer Center under project PAS0239.

REFERENCES

1. Reid, L., Moore, R. D., 1978, "Performance of Single-Stage Axial-Flow Transonic Compressor with Rotor and Stator Aspect Ratios of 1.19 and 1.26 Respectively, and With Design Pressure Ratio of 1.82," *NASA Technical Report No. TP-1338*.

2. Bright, M. M., Qammar, H. K., Wang, L., 1999, "Investigation of Pre-Stall Mode and Pip Inception in High-Speed Compressors Through the Use of

Correlation Integral," *ASME J. Turbomach.*, **121**, pp. 743-750.

3. Camp, T. R., Day, I. J., 1997, "A Study of Spike and Modal Stall Phenomena in a Low Speed Axial Compressor," *ASME J. Turbomach.*, **120**, pp. 393-401.
4. Weichert, S., Day, I., 2013, "Detailed Measurements of Spike Formation in an Axial Compressor," *ASME J. Turbomach.*, **136**(5), p. 051006.
5. McDougall, N. M., 1988, "Stall Inception in Axial Compressors," *Ph.D. Thesis*, Cambridge University, Cambridge.
6. Garnier, V. H., Epstien, A., Greitzer, E. M., 1991, "Rotating Waves as a Stall Inception Indication in Axial Compressors," *ASME J. Turbomach.*, **113**, pp. 290-301.
7. Day, I. J., 1993, "Stall Inception in Axial Flow Compressors," *ASME J. Turbomach.*, **115**, pp. 1-9.
8. Suder, K. L., Celestina, M. L., 1996, "Experimental and Computational Investigation of the Tip Clearance Flow in a Transonic Axial Compressor Rotor," *ASME J. Turbomach.*, **118**, pp 218-229.
9. Hendricks, G. J., Bonnaure, L. P., Longley, J. P., Greitzer, E. M., Epstein, A. H., 1993, "Analysis of Rotating Stall Onset in High Speed Axial Flow Compressor," *AIAA Paper No. 93-2233*.
10. Suder, K. L., Hathaway, M. D., Thorp, S. A., Strazisar, A. J., Bright, M. B., 2001, "Compressor Stability Enhancement Using Discrete Tip Injection," *ASME J. Turbomach.*, **123**, pp 14-23.
11. Weigle, H. J., Paduano, J. D., Frechette, L. G., Epstein, A. H., Greitzer, E. M., Bright, M. M., and Strazisar, A. J., 1998, "Active stabilization of Rotating Stall and Surge in a Transonic Single Stage Axial Compressor," *ASME J. Turbomach.*, **120**(4), pp 625-636.
12. Yamada, K., Funazaki, K., Sasaki, H., 2008, "Numerical Investigation of Relation Between Unsteady Behavior of Tip Leakage Vortex and Rotating Disturbance in a Transonic Axial Compressor Rotor," *ASME Turbo Expo Paper No. GT2008-50779*.
13. Khaleghi, H., 2015, "Stall Inception and Control in a Transonic Fan, Part A: Rotating Stall Inception," *Aero. Sci. Tech.*, **41**, pp. 250-258.
14. Chen, J. P., Hathaway, M. D., Herrick, G. P., 2008 "Pre-stall Behavior of a Transonic Axial Compressor Stage via Time-Accurate Numerical Simulation," *ASME J. Turbomach.*, **130**(4), p. 041014.
15. Hah, C., Rabe, D. C., Wadia, A. R., 2004, "Role of Tip-Leakage Vortices and Passage Shock in Stall Inception in a Swept Transonic Compressor Rotor," *ASME Turbo Expo Paper No. GT2004-53867*.
16. Schleichriem, S., Lötzerich, M., 1997, "Breakdown of Tip Leakage Vortices in Compressors at Flow Conditions Close to Stall," *ASME IGTA Paper No. 97-GT-41*.

17. Vo, H. D., Tan, C. S., Greitzer, E. M., "Criteria for spike initiated Rotating Stall," *ASME J. Turbomach.*, **130**(1), p.011023.
18. Zhang, Y., Lu, X., Chu, W., Zhu, J., 2010, "Numerical Investigation of the Unsteady Tip Leakage Flow and Rotating Stall Inception in a Transonic Compressor," *J. Therm. Sci.*, **19**(4), pp. 310-317.
19. Chen, J. P., Webster, R. S., Hathaway, M. D., Herrick, G. P., Skoch, G. J., 2009, "High Performance Computing of Compressor Rotating Stall and Stall Control," *Int. Comp. Aided Eng.*, **16**, pp. 75-89.
20. Yamada, K., Funazaki, Furukawa, M., 2007, "The Behavior of Tip Clearance Flow at Near-Stall Condition in a Transonic Axial Compressor Rotor," *ASME Turbo Expo Paper No. GT2007-27725*.
21. Copenhaver, W. W., Mayhew, E. R., Hah, C., Wadia, A. R., 1996, "The Effects of Tip Clearance on a Swept Transonic Compressor Rotor," *ASME J. Turbomach.*, **118**, pp. 230-239.
22. Aggarawal, C. C., 2013, "Outlier Analysis," *Springer*, New York.
23. Hodge, V., Austin, J., 2004, "A Surevey of Outlier Detection Methodologies," *Artif. Intell. Rev.*, **22**(2), pp. 85-126.
24. Dean, R. B., Dixon, W. J., 1951 "Simplified Statistics for Small Numbers of Observations," *Anal. Chem.*, **23**(4), pp. 636-638.
25. Chandola, V., Banerjee, A., Kumar, V., 2009, "Anomaly Dectection: A Survey," *ACM Comput. Surv.*, **41**(3), pp. 1-58 .
26. Grubbs, F. E., 1950, "Sample Criteria for testing outlying observations," *Annals of Math. Stat.*, pp. 27-58.
27. Chen, C. M., Dutta, S., Liu, X., Heinlein, G. S., Shen, H. W., Chen, J. P., 2016, "Visualization and Analysis of Rotating Stall for Transonic Jet Engine Simulation," *IEEE Trans. Vis. Comp. Graph.*, **22**(1), pp. 847-856.
28. Chen, J. P., Whitfield, D. L., 1993, "Navier-Stokes Calculations for the Unsteady Flowfield of Turbomachinery," *AIAA Paper No. AIAA-93-0676*.
29. Kirtley, K. R., Beach, T. A., Adamczyk, J. J., 1990, "," *AIAA Paper No. AIAA-90-2356*.
30. Chima, R. V., 1998, "Calculation of Tip Clearance Effects in a Transonic Compressor Rotor," *ASME J. Turbomach.*, **120**, pp 131-140.
31. Shabbir, A., Zhu, J., Celestina, M., 1998, "Assessment of Three Turbulence Models in a Compressor Rotor," *ASME Paper No. 96-GT-198*.
32. Althaus, W., Krause, E., Hofhaus, J., Weimer, M., 1994, "Vortex Breakdown: Transition Between Bubble- and Spiral-Type Breakdown," *Meccanica*, **29**, pp. 373-382.
33. Lucca-Negro, O., O'Doherty, T., 2001, "Vortex Breakdown: a Review," *Prog. Ener. Comb. Sci.*, **27**, pp. 431-481.
34. Ruith, M. R., Chen, P., Meiburg, E., Maxworthy, T., 2003, "Three-Dimensional Vortex Breakdown in Swirling Jets and Wakes: Direct Numerical Simulation," *J. Fluid Mech.*, **486**, pp. 331-378.
35. Qadri, U. A., Mistry, D., Juniper, M. P., 2013, "Structural Sensitivity of Spiral Vortex Breakdown," *J. Fluid Mech.*, **720**, pp. 558-581.